Report

Current Biology

# Doublecortin reinforces microtubules to promote growth cone advance in soft environments

## Graphical abstract

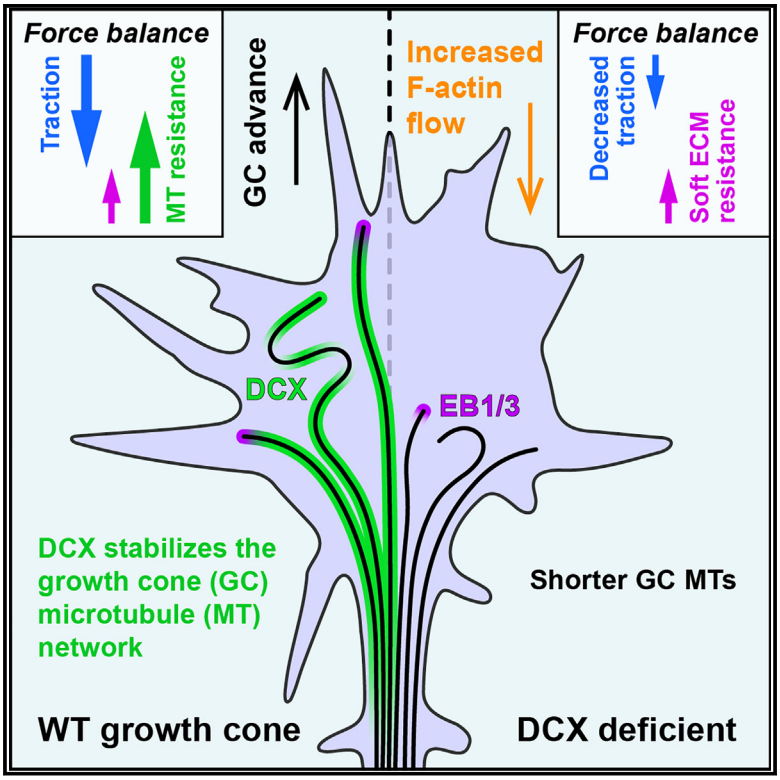


## Highlights

- DCX binds straight microtubules in human cortical neuron growth cones
- DCX stabilizes growth cone microtubules by inhibiting depolymerization
- Growth cone-generated traction stresses are small and transient
- DCX-stabilized microtubules counter contractility to promote growth cone advance

## Authors

Alessandro Dema, Rabab A. Charafeddine, Jeffrey van Haren, ..., Kyle A. Jacobs, Matthew L. Kutys, Torsten Wittmann

## Correspondence

torsten.wittmann@ucsf.edu

## In brief

Mutations in doublecortin (DCX), a microtubule-associated protein in immature neurons, can cause brain malformations. Dema et al. show that DCX binds and stabilizes straight growth cone microtubules in hiPSC-derived cortical neurons and propose that these microtubules mechanically support growth cone advance in physiologically soft surroundings.

Dema et al., 2024, Current Biology *34*, 5822–5832
December 16, 2024 
https://doi.org/10.1016/j.cub.2024.10.063

CellPress

CellPress
OPEN ACCESS

Current Biology

Report

# Doublecortin reinforces microtubules to promote growth cone advance in soft environments

Alessandro Dema,[1,2,3] Rabab A. Charafeddine,[1,2] Jeffrey van Haren,[1,4] Shima Rahgozar,[1] Giulia Viola,[1,5] Kyle A. Jacobs,[1] Matthew L. Kutys,[1] and Torsten Wittmann[1,6,*]

[1]Department of Cell & Tissue Biology, University of California, San Francisco, 513 Parnassus Avenue, San Francisco, CA 94143, USA
[2]These authors contributed equally
[3]Present address: Helmholtz Zentrum München, Ingolstädter Landstraße 1, 85764 Neuherberg, Germany
[4]Present address: Department of Cell Biology, Erasmus MC, 3000 CA Rotterdam, the Netherlands
[5]Present address: Institute for Research in Biomedicine (IRB Barcelona), Baldiri Reixac 10, 08028 Barcelona, Spain
[6]Lead contact
*Correspondence: torsten.wittmann@ucsf.edu
https://doi.org/10.1016/j.cub.2024.10.063

## SUMMARY

Doublecortin (DCX) is a microtubule (MT)-associated protein in immature neurons. DCX is essential for early brain development,[1] and DCX mutations account for nearly a quarter of all cases of lissencephaly-spectrum brain malformations[2,3] that arise from a neuronal migration failure through the developing cortex.[4] By analyzing pathogenic DCX missense mutations in non-neuronal cells, we show that disruption of MT binding is central to DCX pathology. In human-induced pluripotent stem cell (hiPSC)-derived cortical i$^3$Neurons, genome edited to express DCX-mEmerald from the endogenous locus, DCX-MT interactions polarize very early during neuron morphogenesis. DCX interacts with MTs through two conserved DCX domains[5,6] that bind between protofilaments and adjacent tubulin dimers,[7] a site that changes conformation during guanosine triphosphate (GTP) hydrolysis.[8] Consequently and consistent with our previous results,[5] DCX specifically binds straight growth cone MTs and is excluded from the GTP/guanosine diphosphate (GDP)-inorganic phosphate (Pi) cap recognized by end-binding proteins (EBs). Comparing MT-bound DCX fluorescence to mEmerald-tagged nanocage standards, we measure approximately one hundred DCX molecules per micrometer growth cone MT. DCX is required for i$^3$Neuron growth cone advance in soft microenvironments that mimic the viscoelasticity of brain tissue, and using high-resolution traction force microscopy, we find that growth cones produce comparatively small and transient traction forces. Given our finding that DCX stabilizes MTs in the growth cone periphery by inhibiting MT depolymerization, we propose that DCX contributes to growth cone biomechanics and reinforces the growth cone cytoskeleton to counteract actomyosin-generated contractile forces in soft physiological environments in which weak and transient adhesion-mediated traction may be insufficient for productive growth cone advance.

## RESULTS AND DISCUSSION

### MT association is central to DCX function

Because most pathogenic doublecortin (DCX) missense mutations occur in one of the two conserved DCX domains,[2,9–12] we expressed EGFP-tagged DCX carrying such mutations in non-neuronal retinal pigment epithelial (RPE) cells and measured microtubule (MT) binding in cells expressing similarly low levels of these constructs (Figure S1). Of the DCX mutations tested, twelve were in the N-terminal DCX domain, primarily responsible for MT binding,[6] and three in the first loop of the C-terminal DCX domain thought to be functionally distinct.[6,13,14] Regardless of whether cryoelectron microscopy (cryo-EM) data predicted these mutations to directly participate in MT interactions or if they were located elsewhere,[6] all fifteen pathogenic missense mutations highly significantly reduced DCX-MT binding (Figures S1C and S2A).

Due to the variability of clinical classification criteria in patients with DCX-related cortical malformations and the sparsity of clinical reports for specific mutations, it was difficult to clearly correlate DCX-MT binding with disease severity. All moderate to severe DCX mutations had <20% residual MT binding compared with wild-type DCX (Figure S2A), and only one DCX mutation (Y125D) completely abolished MT binding. Notably, the mildest clinical phenotypes displayed the highest level of remaining MT binding (S47N and R89G), indicating that MT association is an essential activity for normal DCX function.

### DCX is highly enriched on straight MTs in advancing growth cones

To determine DCX dynamics in developing neurons, we integrated mEmerald at the C terminus of the endogenous DCX locus by CRISPR-Cas9 genome editing in i$^3$N cells (Figure S3A), a human-induced pluripotent stem cell (hiPSC) line expressing neurogenin-2 (Ngn2) from a doxycycline promoter to allow

 

CellPress
OPEN ACCESS

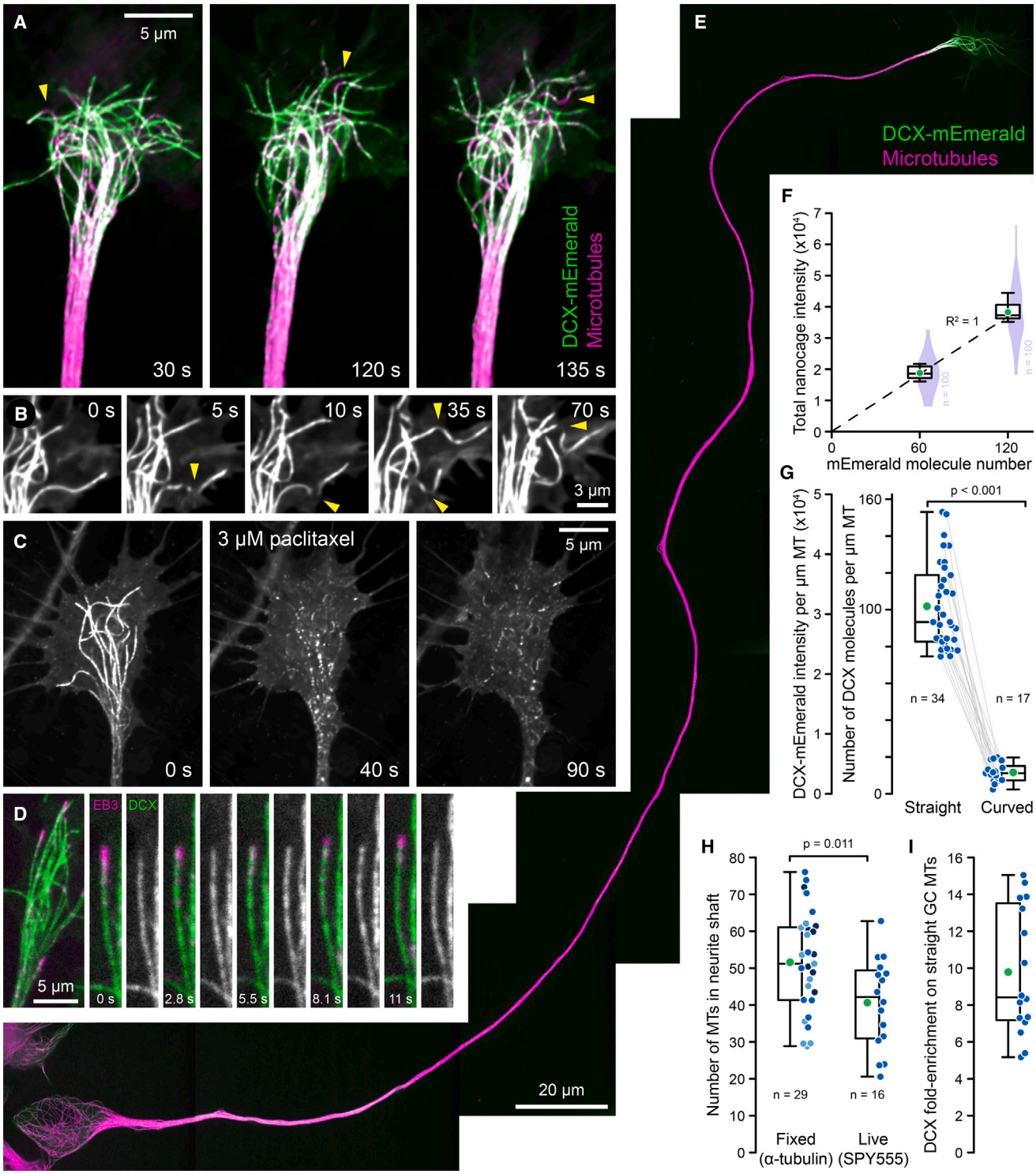


**Figure 1. DCX binds to straight growth cone MTs**

(A) DCX-mEmerald i$^3$Neuron growth cone time-lapse with SPY555-tubulin-labeled microtubules. See also Figure S3 and Video S1.

(B) DCX-mEmerald MTs in a different growth cone. In both (A) and (B), arrows highlight MT buckling and DCX-mEmerald dissociation from bending MT segments. See also Figure S1C.

(C) DCX-mEmerald i$^3$Neuron growth cone after paclitaxel addition showing rapid DCX dissociation from straight MTs.

(D) DCX-mEmerald i$^3$Neuron growth cone expressing TagRFP-EB3, illustrating absence of DCX from growing MT ends.

(E) DCX-mEmerald i$^3$Neuron with a single long axon labeled with SPY555-tubulin, illustrating exclusive DCX enrichment on growth cone MTs. Shown is a composite of eleven images. See also Figures S1–S3 and Videos S2 and S3.

*(legend continued on next page)*

inducible differentiation into cortical glutamatergic i$^3$Neurons.[15,16] Genomic PCR and immunoblotting demonstrated DCX replacement with DCX-mEmerald in the edited i$^3$N line (Figures S3B and S3C), and both proteins were expressed at similar levels. As expected, DCX amounts increased rapidly in both control and edited i$^3$Neurons during early differentiation (Figure S3C). DCX-mEmerald i$^3$Neurons developed normally on laminin, with an average neurite length indistinguishable from control i$^3$Neurons (Figure S3E), and DCX-mEmerald localization was highly polarized. DCX-mEmerald was largely absent from MTs in the cell body or the neurite shaft and predominantly localized to growth cone MTs (Figures 1A, 1E, and S3F–S3I), consistent with overexpression data in rat neurons.[17] DCX-mEmerald reversibly dissociated from growth cone MT segments with high curvature (Figures 1A and 1B; Video S1). Of note, none of the pathogenic DCX mutations appeared to alter this specificity for straight MTs, although this was difficult to evaluate for variants with weak MT binding (Figure S1C). In addition, conversion of the compacted guanosine diphosphate (GDP)-MT lattice to a guanosine triphosphate (GTP)-like expanded state by treating i$^3$Neurons with paclitaxel[8] rapidly dissociated DCX from straight growth cone MTs (Figure 1C), and DCX-mEmerald was absent from the end-binding protein 3 (EB3)-labeled domain at growing MT ends (Figure 1D). This aligns with our previous results in non-neuronal cells[5] and confirms that DCX specifically recognizes straight GDP-MTs at physiological expression levels in developing neurons.

DCX interactions with growth cone MTs were highly dynamic and coincided with the appearance of F-actin-rich protrusions at very early stages of neuron morphogenesis. Within hours of plating pre-differentiated DCX-mEmerald i$^3$Neurons, MTs invading F-actin-rich protrusions were brightly decorated with DCX-mEmerald (Figure S3F; Video S2). DCX-mEmerald disappeared when these exploratory growth cones retracted, and DCX-mEmerald enrichment strongly correlated with growth cone advance both at the end of elongating neurites and at collateral branches (Figures S3F–S3H; Video S3).

Because DCX-mEmerald is expressed from the endogenous promoter and therefore present at near-physiological levels (Figure S3C), we determined how many DCX molecules bound to growth cone MTs by comparing DCX-mEmerald fluorescence to standards with known mEmerald molecule numbers. I3-01 peptides self-assemble into dodecahedron nanocages with one I3-01 trimer at each vertex (Figure S4B), and thus I3-01 peptides tagged with either one or two mEmeralds assemble into nanocages with 60 or 120 mEmerald molecules, respectively.[18,19] Measuring the total fluorescence intensity of such nanocages in transfected RPE cells (Figures S4A and S4C) relates fluorescence intensity to a specific number of mEmerald molecules (Figure 1F). With this calibration, we calculated that straight growth cone MTs bound 102 ± 23 DCX-mEmerald molecules per μm MT (Figures 1G and S4D). Given that DCX has two DCX domains[5,6] and does not bind the MT seam,[7] we estimate a maximum of ∼750 DCX-binding sites per μm MT. Thus, the amount of DCX bound to straight growth cone MTs remains well below saturation.

To compare DCX-MT binding in the growth cone to the neurite shaft, we estimated the number of neurite MTs both in fixed i$^3$Neurons stained for α-tubulin or in live SPY555-tubulin-labeled i$^3$Neurons. Assuming that most staining is MT specific, the ratio of the neurite shaft MT bundle cross-section intensity to the intensity profile across single growth cone MTs yields an approximate number of neurite shaft MTs. Because neurites vary in thickness, some variability in MT number is expected. Nevertheless, both labeling methods produced close estimates of 40–50 neurite shaft MTs (α-tubulin immunofluorescence: 52 ± 14 MTs; SPY555-tubulin: 41 ± 12; Figure 1H). By then comparing the growth cone MT to neurite DCX-mEmerald fluorescence intensity ratio, we estimated that fewer than 10 DCX molecules are present on neurite shaft MT, similar to curved MT segments in growth cones (Figures 1G and 1I).

## Phosphorylation by Cdk5 does not control DCX binding to MTs in cells

To test if phosphorylation spatially controls DCX-MT binding in developing i$^3$Neurons, we determined phosphorylated residues by mass spectrometry of immunoprecipitated DCX-mEmerald (Figure S3D). Although we were unable to obtain complete DCX sequence coverage, the most highly phosphorylated residues in i$^3$Neurons were previously identified cyclin-dependent kinase 5 (Cdk5) sites (S28, S306, S332, and S339; Figure S2B).[20] Because the impact of Cdk5 phosphorylation on DCX-MT binding remains poorly understood, we measured MT binding of DCX-EGFP constructs in which either S28 near the N terminus or all eight C-terminal Cdk5 sites were mutated into phosphomimetic aspartate or glutamate residues (Figures S2C and S2D). However, all Cdk5 phosphorylation site mutations displayed only moderately reduced MT binding in transfected RPE cells, indicating that Cdk5 is not a major regulator of DCX-MT binding.

Although our mass spectrometry did not identify S47 phosphorylation, S47 is directly involved in MT binding,[6] and phosphorylation was previously proposed to reduce DCX-MT binding *in vitro*.[21] We therefore also tested a phosphomimetic S47D DCX-EGFP single amino acid change, which reduced MT

(F) mEmerald nanocage calibration relating molecule number to fluorescence intensity. The linear regression (dashed line) through the medians of 10 cells per condition (with 10 nanocages analyzed per cell) indicates no fluorescence quenching even at high mEmerald densities. Violin plots show the distribution of all nanocage intensity measurements. See also Figure S4.
(G) DCX-mEmerald molecule number quantification on straight and curved growth cone MT segments. Gray lines connect data from the same growth cones.
(H) Estimation of the neurite shaft MT number in fixed or live DCX-mEmerald i$^3$Neurons by comparing individual growth cone MT tubulin label fluorescence to the neurite shaft.
(I) DCX-mEmerald enrichment on straight growth cone MTs compared with neurite shaft MTs using the same SPY555-tubulin DCX-mEmerald i$^3$Neuron dataset as in (H).
(G-I) Boxplots include the mean (green) and all data points (blue).
(G and H) Statistical analysis by paired (G) or unpaired t test (H).

CellPress
OPEN ACCESS

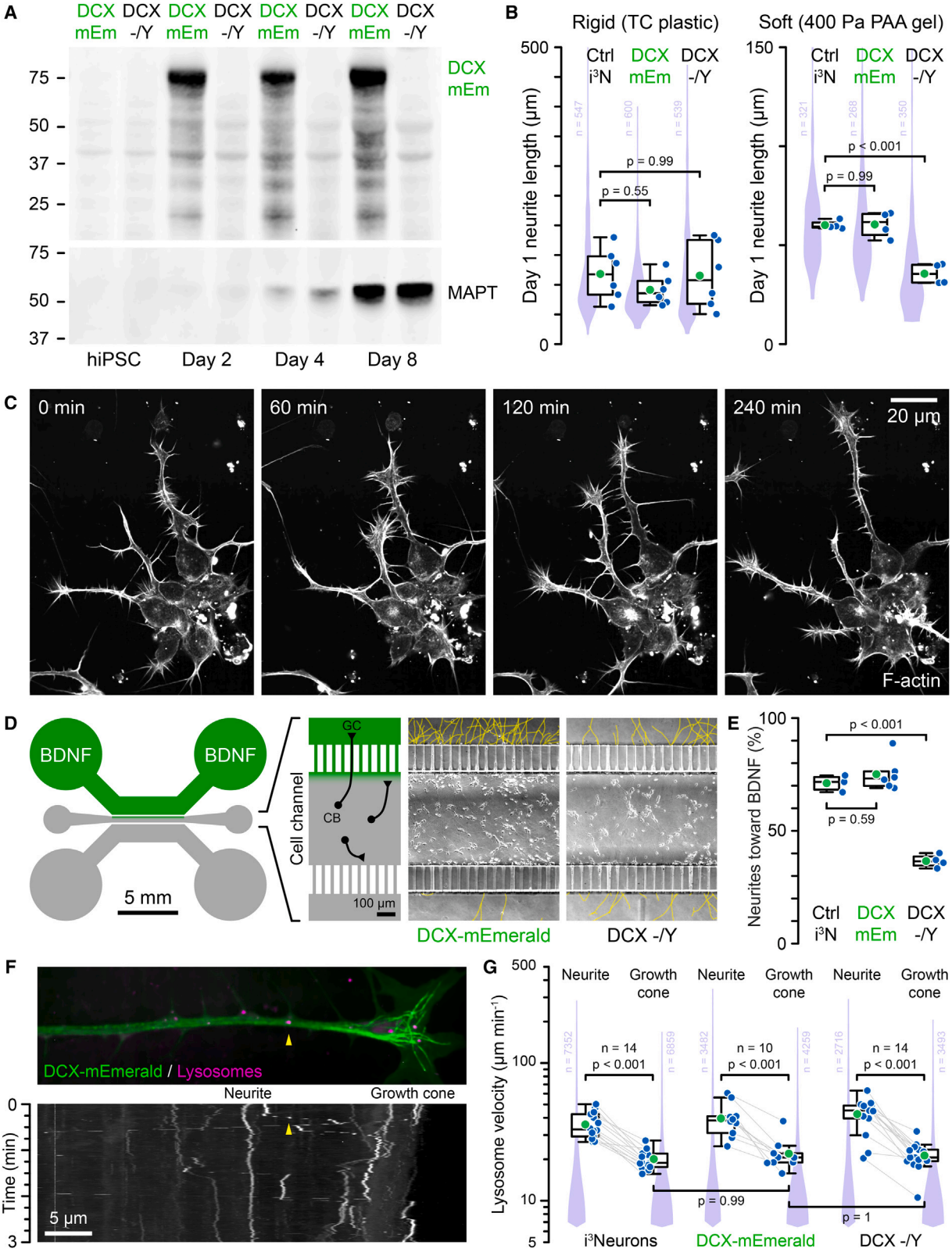


*(legend on next page)*

binding to a much greater extent (9% ± 1% of WT; Figure S2D). Although these data support that S47 phosphorylation, which is not a Cdk5 target, can greatly inhibit DCX-MT association in cells, it remains to be determined if a S47 phosphorylation gradient is responsible for the observed gradient of DCX-MT binding in developing neurons.

## DCX is required for directed growth cone advance in physiological environments

To ask how DCX supports brain development, we introduced a frameshift in DCX exon 1 by CRISPR-Cas9 genome editing. These DCX −/Y i$^3$Neurons no longer expressed DCX, but protein levels of MT-associated protein tau (MAPT) increased normally during i$^3$Neuron differentiation (Figure 2A). Given that DCX was dynamically enriched on MTs in growth cones very early during i$^3$Neuron morphogenesis, we expected a pronounced neurite outgrowth defect in DCX −/Y i$^3$Neurons. To our surprise, however, DCX −/Y i$^3$Neurons formed dynamic growth cones similar to control and DCX-mEmerald i$^3$Neurons (Figure 2C), indicating that DCX is not required to initiate growth cones. In addition, on rigid tissue culture plastic, there was no obvious difference in growth cone morphology or neurite length between control, DCX-mEmerald, and DCX −/Y i$^3$Neurons. However, on soft 400 Pa polyacrylamide (PAA) gels that more closely resemble the viscoelasticity of brain tissue through which neurites navigate during development,[22,23] DCX −/Y neurites remained significantly shorter compared with control or DCX-mEmerald i$^3$Neurons (Figure 2B).

Because dynamic MTs are required for growth cone guidance downstream of chemotactic signaling,[24] we next tested if in addition to this growth cone advance defect in physiological stiffness, DCX −/Y i$^3$Neurons also display a growth cone guidance phenotype. Because growth cones sense gradients of brain-derived neurotrophic factor (BDNF),[25] we analyzed neurite orientation in polydimethylsiloxane (PDMS) devices that directionally present BDNF to developing i$^3$Neurons. Pre-differentiated i$^3$Neurons were plated in the central channel of these devices that are connected to reservoir channels on either side through microchannels that allow growing neurites to pass but for the most part restrict cell body movement (Figure 2D).[26] One of these reservoir channels contained BDNF, and after 1–2 days, a larger number of control or DCX-mEmerald neurites extended into the BDNF channel compared with the channel without BDNF, which was not the case for DCX −/Y i$^3$Neurons (Figure 2E). Together, these data indicate that although a DCX −/Y phenotype was not immediately obvious in standard *in vitro* i$^3$Neuron differentiation conditions, DCX is required for neurite elongation and growth cone guidance in more physiological environments.

## Loss of DCX does not affect lysosome transport

Recent *in vitro* data indicate that DCX on purified MTs greatly inhibits both binding and MT plus end-directed movement of kinesin-1 (KIF5) MT motor proteins.[27] Because KIF5 is the principal motor driving fast anterograde organelle transport in neurons including lysosomes,[28,29] we asked if lysosome dynamics are altered in i$^3$Neurons without DCX. While many large and brightly labeled lysosomes remained in i$^3$Neuron cell bodies, smaller lysosomes rapidly moved along i$^3$Neuron neurite shafts and in and out of growth cones (Figure 2F; Video S4). We tracked motile lysosomes defined as moving faster than 6.5 μm min$^{-1}$ (i.e., 2 pixels/s) and compared lysosome velocity in neurites and growth cones of control, DCX-mEmerald and DCX −/Y i$^3$Neurons. In all three genotypes, lysosomes moved significantly faster in neurite shafts compared with growth cones (i.e., in control i$^3$Neurons, 36 ± 8 μm min$^{-1}$ in the shaft versus 20 ± 3 μm min$^{-1}$ in growth cones). However, there was no detectable change in growth cone lysosome velocity in DCX −/Y i$^3$Neurons (Figure 2G). Thus, even though lysosomes were much less motile in growth cones, which would be consistent with DCX inhibiting transport along growth cone MTs, at physiological expression levels DCX does not reduce lysosome motility, with the caveat that these experiments cannot distinguish between KIF5-mediated transport and other modes of motility.

## DCX protects growth cone MTs from depolymerization

We next asked if DCX is required for growth cone MT organization by analyzing fixed i$^3$Neuron growth cones stained for MTs and F-actin. In control and DCX-mEmerald i$^3$Neurons, MTs extended further into the growth cone periphery compared with DCX −/Y i$^3$Neuron growth cones (Figure 3A), in which the bulk of MTs often remained confined to the central domain.

**Figure 2. DCX is required for growth cone advance in physiological conditions**

(A) DCX-mEmerald (top) and MAPT (bottom) immunoblot during i$^3$Neuron differentiation in DCX-mEmerald and DCX −/Y i$^3$Neurons.

(B) Neurite lengths in control, DCX-mEmerald, and DCX −/Y i$^3$Neurons on either rigid or soft substrates. Boxplots include the mean (green) and all data points (blue) corresponding to the averages from six (rigid) and four (soft) independent experiments, respectively. Violin plots show the distribution of all neurite length measurements.

(C) SPY555-FastAct labeled DCX −/Y i$^3$Neuron neurite outgrowth dynamics.

(D) Diagram of the PDMS device used to measure i$^3$Neuron neurite growth toward BDNF. Pre-differentiated i$^3$Neurons are plated in medium without BDNF into a central channel that is connected to two reservoir channels on either side by microchannels that allow growth cones (GCs) to pass through but confine cell bodies (CBs) to the central channel. One of the reservoir channels is filled with medium containing 10 ng/mL BDNF. Representative images show DCX-mEmerald and DCX −/Y i$^3$Neurons in the central chemotaxis channel 2 days after plating. Neurites growing through the microchannels are highlighted by yellow lines. Note the higher density of DCX-mEmerald neurites in the top reservoir channel with BDNF.

(E) Quantification of the fraction of neurites growing into the BDNF channel versus the other channel without BDNF. Boxplots include the mean (green) and all data points (blue) from independent experiments.

(F) Lysosomes labeled with silicon rhodamine (SiR)-lysosome in a DCX-mEmerald i$^3$Neuron. The top panel shows a single frame of a time-lapse sequence, and the bottom panel a kymograph of lysosome movement. The arrow highlights a fast-moving lysosome in both panels. See also Video S4.

(G) Comparison of lysosome velocity in the neurite and the growth cone of control, DCX-mEmerald and DCX −/Y i$^3$Neurons. Boxplots include the mean (green) and average velocity measurements from 10 to 14 i$^3$Neurons per genotype (blue). Gray lines connect data from the same i$^3$Neurons. Violin plots show the distribution of all frame-to-frame lysosome velocity measurements.

Statistical analysis in (B), (E), and (G) by ANOVA with Tukey-Kramer honest significant difference (HSD).

CellPress
OPEN ACCESS

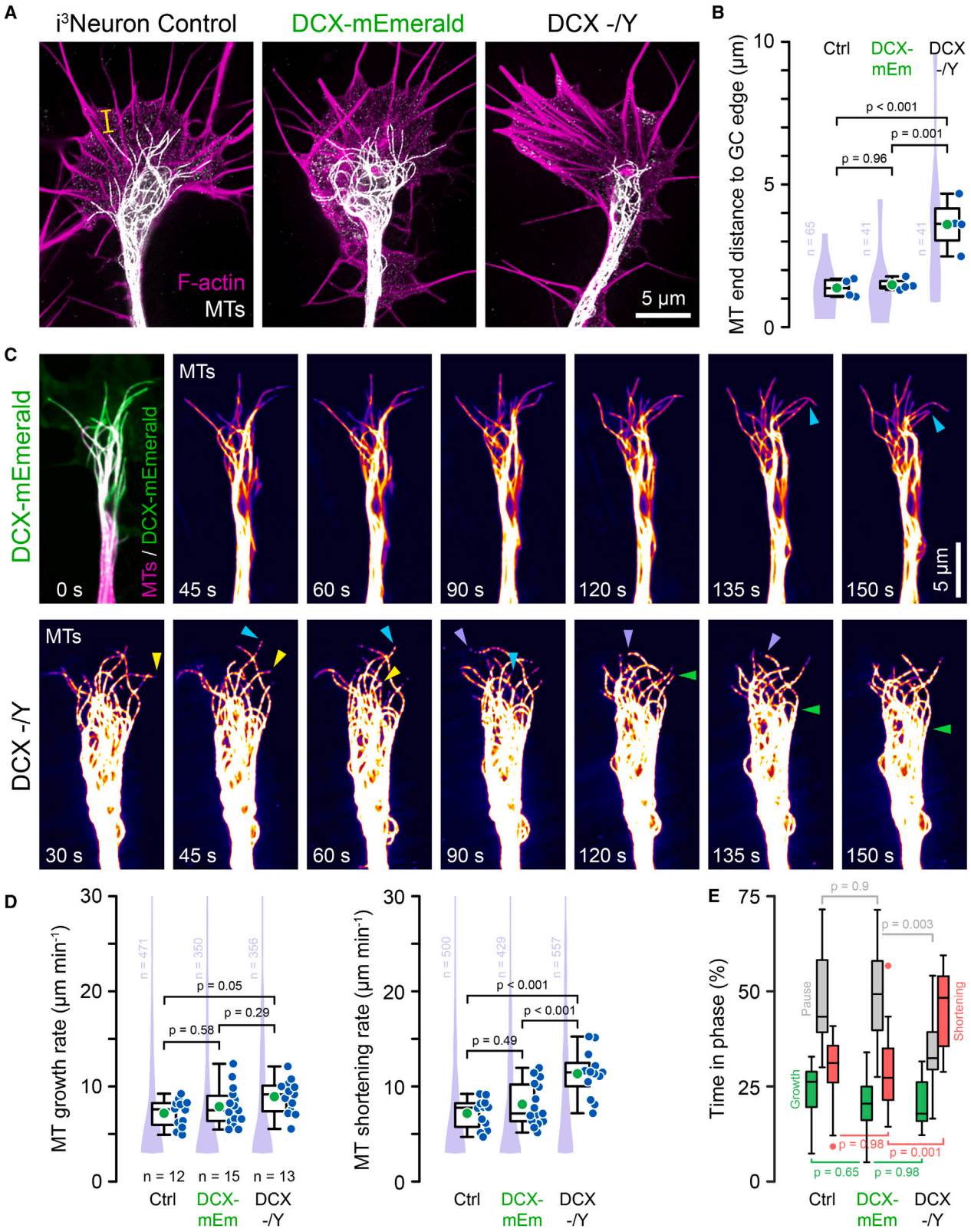


**Figure 3. DCX stabilizes growth cone MTs**

(A) Representative immunofluorescence images of MTs in control, DCX-mEmerald, and DCX −/Y i³Neuron growth cones stained with anti-tubulin antibodies and fluorescent phalloidin.

*(legend continued on next page)*

We quantified this by measuring the distance of the longest three MTs to the edge of the growth cone lamellipodial veil, which more than doubled in DCX −/Y i$^3$Neurons (Figure 3B).

By using Spy555-tubulin at very low concentrations, we then analyzed how DCX impacts growth cone MT polymerization dynamics (Figure 3C; Video S5).[16] As expected, because DCX is absent from growing MT ends (Figure 1D), the MT growth rate was minimally affected in DCX −/Y i$^3$Neurons. By contrast, the MT shortening rate was significantly increased in DCX −/Y (11.3 ± 2.3 μm min$^{-1}$) compared with control (7.2 ± 1.5 μm min$^{-1}$) and DCX-mEmerald i$^3$Neurons (8.1 ± 2.2 μm min$^{-1}$) (Figure 3D), similar to non-neuronal DCX-expressing cells.[5] In addition, and consistent with DCX inhibiting MT depolymerization, the fraction of time growth cone MTs spent in a shortening phase was nearly doubled in DCX −/Y i$^3$Neurons while the time MTs spent growing was unaffected (Figure 3E). Together, these data indicate that DCX promotes and stabilizes MT extension into the growth cone periphery primarily by protecting MTs from shortening and slowing the depolymerization rate.

## DCX-stabilized MTs counteract contractile forces to enable growth cone advance

Because MTs buckle due to coupling to F-actin retrograde flow,[30,31] similar to the buckling of DCX-covered MTs we observe in DCX-mEmerald i$^3$Neurons (Figures 1A and 1B; Video S1), we examined how the reduction of growth cone MTs in DCX −/Y i$^3$Neurons impacted growth cone F-actin dynamics. Using SPY650-FastAct at low concentrations, we measured F-actin retrograde flow rates (Figures 4A and 4B; Video S6), which in control (2.9 ± 0.1 μm min$^{-1}$) and DCX-mEmerald i$^3$Neurons (2.9 ± 0.04 μm min$^{-1}$) were nearly identical to what we reported previously.[16] By contrast, F-actin retrograde flow was doubled in DCX −/Y i$^3$Neurons (6.6 ± 0.5 μm min$^{-1}$), indicating that DCX-stabilized growth cone MTs counteract F-actin retrograde flow.

Because F-actin retrograde flow is linked to force transduction to the extracellular matrix,[32] we analyzed i$^3$Neuron-generated forces by high-resolution time-lapse traction force microscopy (TFM) on soft 400 Pa PAA gels (Figures 4C and 4D), which revealed transient traction stresses predominantly localized near the edge of i$^3$Neuron growth cones as well as along filopodia that generally remained below 100 Pa (Figure 4E). Although it is difficult to compare traction stress measurements between different experimental studies, the average traction stresses of 10–20 Pa exerted by human i$^3$Neuron growth cones are similar to data from rat central nervous system neurons,[33–35] but orders of magnitude smaller than traction stresses produced by fibroblasts or other types of migrating adherent cells.[36–39] Because local traction stress increases at the growth cone edge coincided with bending of DCX-coated MTs in DCX-mEmerald i$^3$Neurons (Figure 4C; Video S7), we asked how i$^3$Neuron-generated traction stress changed in the absence of DCX. Indeed, the average traction stress in DCX −/Y i$^3$Neuron growth cones was significantly reduced, and the decrease in strain energy, i.e., the work growth cones exert to deform the substrate, was even more pronounced (control: 0.29 ± 0.19 fJ; DCX −/Y: 0.1 ± 0.05 fJ; Figures 4D and 4F; Video S8). By contrast, we did not find a significant difference in either the duration or magnitude of transient traction stresses exerted by individual filopodia (peak force: control: 0.2 ± 0.16 nN; DCX −/Y: 0.15 ± 0.11 nN; Figure 4G), indicating that DCX does not directly influence force generation.

Due to their tubular geometry, MTs are the stiffest cytoskeleton polymer, and when crosslinked to the F-actin cytoskeleton, individual MTs can bear compressive loads exceeding 100 pN.[40] We therefore propose that the DCX-stabilized growth cone MT cytoskeleton acts as an intracellular mechanical component to resist and counteract actomyosin-mediated contractility in the highly compliant developing central nervous system in which adhesion-mediated traction may be insufficient to support persistent growth cone advance. Consistent with the F-actin retrograde flow increase in the absence of DCX, crosslinking of DCX-stabilized MTs to the F-actin cytoskeleton likely contributes to this intracellular clutch mechanism and complements the extracellular adhesion clutch that couples contractile forces to transmembrane, integrin-mediated adhesion sites[41,42] that in growth cones are generally very small.[43] DCX-mediated stabilization of growth cone MT length and number may by itself account for a greater compression resistance of the growth cone cytoskeleton. However, because DCX is specific for straight MTs, it is possible that MT-bound DCX also actively stiffens MTs, which is supported by MTs appearing straighter in cells overexpressing DCX.[5,17] If this is relevant at physiological DCX levels remains to be determined. Alternatively, DCX may protect MTs from mechanical damage, as growth cone MTs from DCX knockout mouse neurons accumulate MT wall defects,[44] which could explain the decreased growth cone MT stability without DCX.

## RESOURCE AVAILABILITY

### Lead contact

Requests for further information and resources should be directed to and will be fulfilled by the lead contact, Torsten Wittmann (torsten.wittmann@ucsf.edu).

(B) Comparison of the average shortest distance between the ends of the three longest MTs from the growth cone edge as illustrated by the yellow line in (A). Boxplots include the mean (green) and all data points (blue) corresponding to 10–15 growth cones from four independent experiments. Violin plots show the distribution of measurements from all growth cones.

(C) SPY555-tubulin-labeled growth cone MT dynamics in DCX-mEmerald and DCX −/Y i$^3$Neurons. To better visualize individual growth cone MTs, images are shown in pseudo-color. Colored arrows highlight shortening MTs, illustrating that MTs depolymerize faster and more frequently in DCX −/Y i$^3$Neurons. Note that MTs appear speckled due to the very low concentration of SPY555-tubulin used in these experiments. See also Video S5.

(D) Quantification of growth cone MT growth and shortening rates in control, DCX-mEmerald, and DCX −/Y i$^3$Neurons. Boxplots include the mean (green) and all data points (blue) corresponding to the averages from 12 to 15 growth cones per condition. Violin plots show the distribution of all frame-to-frame rate measurements.

(E) Quantification of the fraction of time growth cone MT ends spend in growth, pause, or shortening phases with a pause defined as less than 150 nm (3 pixel) frame-to-frame displacement showing a shift toward more frequent shortening events in DCX −/Y i$^3$Neurons.

Statistical analysis in (B), (D), and (E) by ANOVA with Tukey-Kramer HSD.

CellPress
OPEN ACCESS

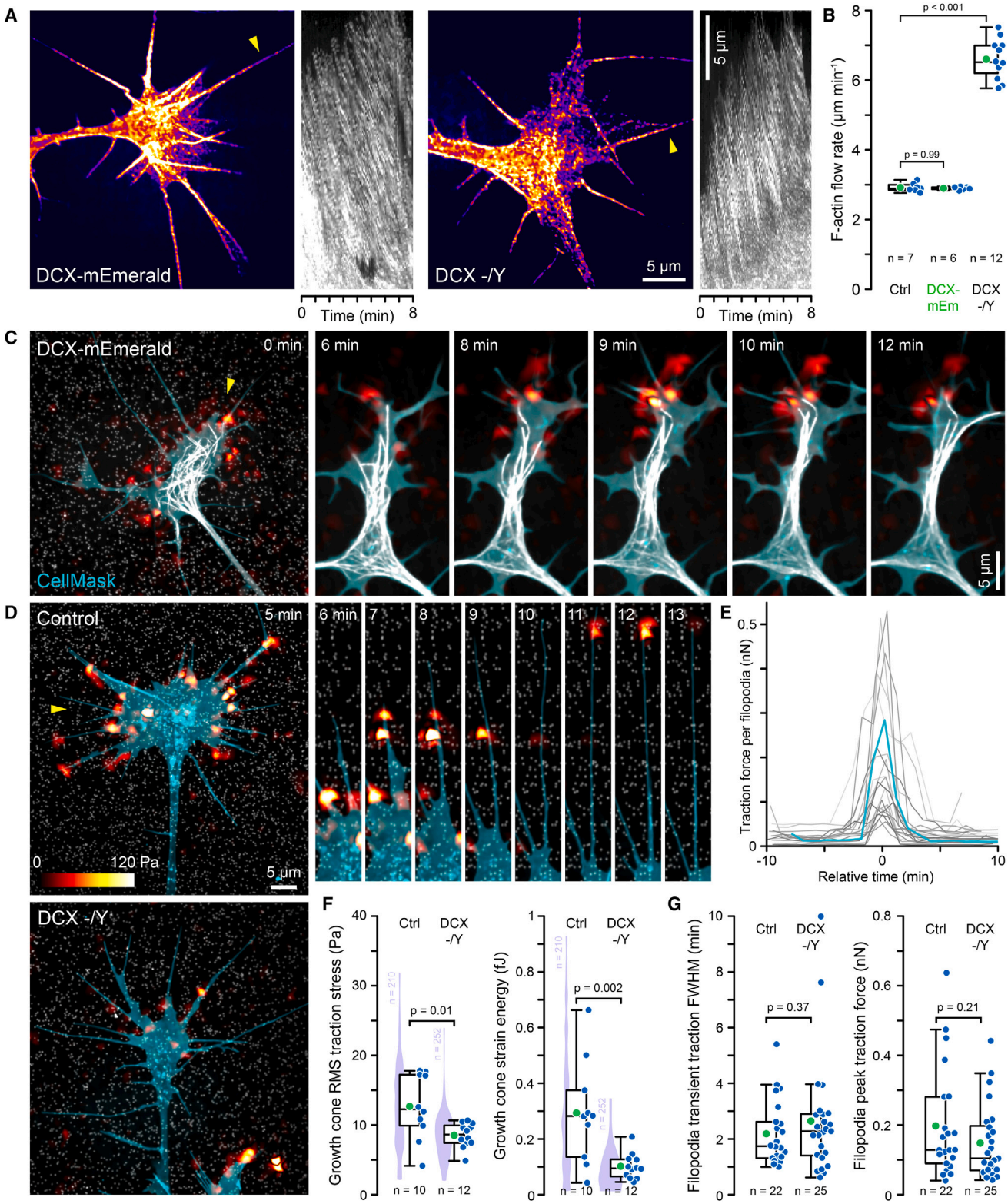


**Figure 4. DCX-coated growth cone MTs counteract actomyosin contractility**

(A) Growth cones of DCX-mEmerald and DCX −/Y i$^3$Neurons labeled with SPY650-FastAct that binds to F-actin and kymographs along the filopodia indicated by arrows. See also Video S6.

*(legend continued on next page)*

### Materials availability

All unique/stable reagents generated in this study are available from the lead contact without restriction. Relevant plasmids will also be deposited to Addgene.

### Data and code availability

- Microscopy and analysis data used to generate the figures in this paper have been deposited to Dryad and are publicly available as of the date of publication at https://doi.org/10.5061/dryad.8sf7m0d01.
- Any additional information required to reanalyze the data reported in this paper is available from the lead contact upon reasonable request.

## ACKNOWLEDGMENTS

We thank Li Gan for the i$^3$N hiPSCs, Matthew Akamatsu for nanocage constructs, and William Dobyns for discussing DCX pathologies. This work was supported by National Institutes of Health grants R01 NS107480, S10 RR026758, and S10 OD028611 to T.W.; funding from the UCSF Research Allocation Program; American Epilepsy Society Fellowship CA-0122654 to R.A.C.; and Tobacco-Related Disease Research Program Predoctoral Fellowship T33DT6442 and National Science Foundation Graduate Research Fellowship 2038436 to K.A.J.

## AUTHOR CONTRIBUTIONS

Conceptualization, A.D., R.A.C., J.v.H., and T.W.; methodology, A.D., R.A.C., J.v.H., K.A.J., M.L.K., and T.W.; software, T.W.; investigation, A.D., R.A.C., S.R., G.V., and T.W.; writing – original draft, T.W.; writing – review and editing, A.D., R.A.C., J.v.H., and T.W.; funding acquisition, T.W.; supervision, T.W.

## DECLARATION OF INTERESTS

The authors declare no competing interests.

## STAR★METHODS

Detailed methods are provided in the online version of this paper and include the following:

- KEY RESOURCES TABLE
- EXPERIMENTAL MODEL AND SUBJECT DETAILS
  - Cell lines and cell culture
- METHOD DETAILS
  - Molecular cloning
  - i$^3$N genome editing
  - Antibodies
  - Live microscopy and image analysis
  - Chemotaxis assay
  - Traction force microscopy
- QUANTIFICATION AND STATISTICAL ANALYSIS

## SUPPLEMENTAL INFORMATION

Supplemental information can be found online at https://doi.org/10.1016/j.cub.2024.10.063.

Received: March 27, 2024
Revised: August 5, 2024
Accepted: October 24, 2024
Published: December 2, 2024

## REFERENCES

1. Gleeson, J.G., Lin, P.T., Flanagan, L.A., and Walsh, C.A. (1999). Doublecortin is a microtubule-associated protein and is expressed widely by migrating neurons. Neuron *23*, 257–271. https://doi.org/10.1016/S0896-6273(00)80778-3.
2. Bahi-Buisson, N., Souville, I., Fourniol, F.J., Toussaint, A., Moores, C.A., Houdusse, A., Lemaitre, J.Y., Poirier, K., Khalaf-Nazzal, R., Hully, M., et al. (2013). New insights into genotype–phenotype correlations for the doublecortin-related lissencephaly spectrum. Brain *136*, 223–244. https://doi.org/10.1093/brain/aws323.
3. Di Donato, N., Timms, A.E., Aldinger, K.A., Mirzaa, G.M., Bennett, J.T., Collins, S., Olds, C., Mei, D., Chiari, S., Carvill, G., et al. (2018). Analysis of 17 genes detects mutations in 81% of 811 patients with lissencephaly. Genet. Med. *20*, 1354–1364. https://doi.org/10.1038/GIM.2018.8.
4. Edey, J., Soleimani-Nouri, P., Dawson-Kavanagh, A., Imran Azeem, M.S., and Episkopou, V. (2023). X-linked neuronal migration disorders: gender differences and insights for genetic screening. Int. J. Dev. Neurosci. *83*, 581–599. https://doi.org/10.1002/JDN.10290.
5. Ettinger, A., van Haren, J., Ribeiro, S.A., and Wittmann, T. (2016). Doublecortin is excluded from growing microtubule ends and recognizes the GDP-microtubule lattice. Curr. Biol. *26*, 1549–1555. https://doi.org/10.1016/j.cub.2016.04.020.
6. Manka, S.W., and Moores, C.A. (2020). Pseudo-repeats in doublecortin make distinct mechanistic contributions to microtubule regulation. EMBO Rep. *21*, e51534. https://doi.org/10.15252/embr.202051534.
7. Fourniol, F.J., Sindelar, C.V., Amigues, B., Clare, D.K., Thomas, G., Perderiset, M., Francis, F., Houdusse, A., and Moores, C.A. (2010). Template-free 13-protofilament microtubule-MAP assembly visualized at 8 Å resolution. J. Cell Biol. *191*, 463–470. https://doi.org/10.1083/jcb.201007081.
8. Alushin, G.M., Lander, G.C., Kellogg, E.H., Zhang, R., Baker, D., and Nogales, E. (2014). High-Resolution microtubule structures reveal the structural transitions in αβ-tubulin upon GTP hydrolysis. Cell *157*, 1117–1129. https://doi.org/10.1016/j.cell.2014.03.053.
9. des Portes, V., Francis, F., Pinard, J.M., Desguerre, I., Moutard, M.L., Snoeck, I., Meiners, L.C., Capron, F., Cusmai, R., Ricci, S., et al. (1998). Doublecortin is the major gene causing X-linked subcortical laminar

(B) Quantification of the F-actin retrograde flow rate in growth cones with and without DCX. Boxplots include the mean (green) and all data points (blue) corresponding to at least three flow measurements per growth cone. Statistical analysis by ANOVA with Tukey-Kramer HSD.
(C) Traction force microscopy of a representative DCX-mEmerald i$^3$Neuron growth cone. DCX-mEmerald on growth cone MTs is shown in white. See also Video S7.
(D) Traction force microscopy of control and DCX −/Y i$^3$Neuron growth cones. The time-lapse sequence shows transient traction stress peaks along the filopodia in the control i$^3$Neuron. In both (C) and (D), the CellMask-labeled growth cone is cyan, the polyacrylamide-embedded beads that serve as fiduciary marks to measure gel deformation are gray (omitted from the time-lapse in C), and the traction stress map is shown with the same 0–120 Pa color scale. Time-lapse sequences are 1.5× magnified and their location indicated by arrowheads in the images to the left. See also Video S8.
(E) Overlay of 22 filopodia traction force transients aligned to the peak force position determined by Gaussian fits. The cyan trace corresponds to the filopodium in the time-lapse in (D) at 7–9 min.
(F) Quantification of growth cone root mean square (RMS) traction stress averages and strain energies. Boxplots include the mean (green) and all data points (blue) corresponding to the average of 21 time points for each growth cone analyzed. Violin plots show the distribution of measurements from all time points of all growth cones.
(G) Full width at half maximum (FWHM, i.e., duration) and peak forces of filopodia traction stress transients determined by Gaussian fits of individual force traces. Statistical analysis in (F) and (G) by unpaired t test.

heterotopia (SCLH). Hum. Mol. Genet. *7*, 1063–1070. https://doi.org/10.1093/HMG/7.7.1063.

10. Leger, P.L., Souville, I., Boddaert, N., Elie, C., Pinard, J.M., Plouin, P., Moutard, M.L., Des Portes, V., Van Esch, H., Joriot, S., et al. (2008). The location of DCX mutations predicts malformation severity in X-linked lissencephaly. Neurogenetics *9*, 277–285. https://doi.org/10.1007/S10048-008-0141-5.
11. Gleeson, J.G., Minnerath, S.R., Fox, J.W., Allen, K.M., Luo, R.F., Hong, S.E., Berg, M.J., Kuzniecky, R., Reitnauer, P.J., Borgatti, R., et al. (1999). Characterization of Mutations in the Gene doublecortin in Patients with Double Cortex Syndrome. Ann. Neurol. *45*, 146–153. https://doi.org/10.1002/1531-8249.
12. Pilz, D.T., Kuc, J., Matsumoto, N., Bodurtha, J., Bernadi, B., Tassinari, C.A., Dobyns, W.B., and Ledbetter, D.H. (1999). Subcortical band heterotopia in rare affected males can be caused by missense mutations in DCX (XLIS) or LIS1. Hum. Mol. Genet. *8*, 1757–1760. https://doi.org/10.1093/HMG/8.9.1757.
13. Bechstedt, S., and Brouhard, G.J. (2012). Doublecortin recognizes the 13-protofilament microtubule cooperatively and tracks microtubule ends. Dev. Cell *23*, 181–192. https://doi.org/10.1016/j.devcel.2012.05.006.
14. Rafiei, A., Cruz Tetlalmatzi, S.C., Edrington, C.H., Lee, L., Crowder, D.A., Saltzberg, D.J., Sali, A., Brouhard, G.J., and Schriemer, D.C. (2022). Doublecortin engages the microtubule lattice through a cooperative binding mode involving its C-terminal domain. eLife *11*, e66975. https://doi.org/10.7554/ELIFE.66975.
15. Wang, C., Ward, M.E., Chen, R., Liu, K., Tracy, T.E., Chen, X., Xie, M., Sohn, P.D., Ludwig, C., Meyer-Franke, A., et al. (2017). Scalable production of iPSC-derived human neurons to identify tau-lowering compounds by high-content screening. Stem Cell Rep. *9*, 1221–1233. https://doi.org/10.1016/j.stemcr.2017.08.019.
16. Dema, A., Charafeddine, R., Rahgozar, S., van Haren, J., and Wittmann, T. (2023). Growth cone advance requires EB1 as revealed by genomic replacement with a light-sensitive variant. eLife *12*, e84143. https://doi.org/10.7554/ELIFE.84143.
17. Jean, D.C., Baas, P.W., and Black, M.M. (2012). A novel role for doublecortin and doublecortin-like kinase in regulating growth cone microtubules. Hum. Mol. Genet. *21*, 5511–5527. https://doi.org/10.1093/HMG/DDS395.
18. Hsia, Y., Bale, J.B., Gonen, S., Shi, D., Sheffler, W., Fong, K.K., Nattermann, U., Xu, C., Huang, P.S., Ravichandran, R., et al. (2016). Design of a hyperstable 60-subunit protein dodecahedron. [corrected]. Nature *535*, 136–139. https://doi.org/10.1038/NATURE18010.
19. Akamatsu, M., Vasan, R., Serwas, D., Ferrin, M.A., Rangamani, P., and Drubin, D.G. (2020). Principles of self-organization and load adaptation by the actin cytoskeleton during clathrin-mediated endocytosis. eLife *9*, e49840. https://doi.org/10.7554/ELIFE.49840.
20. Tanaka, T., Serneo, F.F., Tseng, H.C., Kulkarni, A.B., Tsai, L.H., and Gleeson, J.G. (2004). Cdk5 phosphorylation of doublecortin Ser297 regulates its effect on neuronal migration. Neuron *41*, 215–227. https://doi.org/10.1016/S0896-6273(03)00852-3.
21. Schaar, B.T., Kinoshita, K., and McConnell, S.K. (2004). Doublecortin microtubule affinity is regulated by a balance of kinase and phosphatase activity at the leading edge of migrating neurons. Neuron *41*, 203–213. https://doi.org/10.1016/S0896-6273(03)00843-2.
22. Tyler, W.J. (2012). The mechanobiology of brain function. Nat. Rev. Neurosci. *13*, 867–878. https://doi.org/10.1038/nrn3383.
23. Guimarães, C.F., Gasperini, L., Marques, A.P., and Reis, R.L. (2020). The stiffness of living tissues and its implications for tissue engineering. Nat. Rev. Mater. *5*, 351–370. https://doi.org/10.1038/s41578-019-0169-1.
24. Suter, D.M., Schaefer, A.W., and Forscher, P. (2004). Microtubule dynamics are necessary for Src family kinase-dependent growth cone steering. Curr. Biol. *14*, 1194–1199. https://doi.org/10.1016/J.CUB.2004.06.049.
25. Li, X., Shim, S., Hardin, K.R., Vanaja, K.G., Song, H., Levchenko, A., Ming, G.L., and Zheng, J.Q. (2022). Signal amplification in growth cone gradient sensing by a double negative feedback loop among PTEN, PI(3,4,5)P3 and actomyosin. Mol. Cell. Neurosci. *123*, 103772. https://doi.org/10.1016/J.MCN.2022.103772.
26. Taylor, A.M., Blurton-Jones, M., Rhee, S.W., Cribbs, D.H., Cotman, C.W., and Jeon, N.L. (2005). A microfluidic culture platform for CNS axonal injury, regeneration and transport. Nat. Methods *2*, 599–605. https://doi.org/10.1038/NMETH777.
27. Monroy, B.Y., Tan, T.C., Oclaman, J.M., Han, J.S., Simó, S., Niwa, S., Nowakowski, D.W., McKenney, R.J., and Ori-McKenney, K.M. (2020). A combinatorial MAP code dictates polarized microtubule transport. Dev. Cell *53*, 60–72.e4. https://doi.org/10.1016/J.DEVCEL.2020.01.029.
28. Cabukusta, B., and Neefjes, J. (2018). Mechanisms of lysosomal positioning and movement. Traffic *19*, 761–769. https://doi.org/10.1111/TRA.12587.
29. Pu, J., Guardia, C.M., Keren-Kaplan, T., and Bonifacino, J.S. (2016). Mechanisms and functions of lysosome positioning. J. Cell Sci. *129*, 4329–4339. https://doi.org/10.1242/JCS.196287/265250/AM/MECHANISMS-AND-FUNCTIONS-OF-LYSOSOME-POSITIONING.
30. Wittmann, T., Bokoch, G.M., and Waterman-Storer, C.M. (2003). Regulation of leading edge microtubule and actin dynamics downstream of Rac1. J. Cell Biol. *161*, 845–851. https://doi.org/10.1083/JCB.200303082.
31. Schaefer, A.W., Kabir, N., and Forscher, P. (2002). Filopodia and actin arcs guide the assembly and transport of two populations of microtubules with unique dynamic parameters in neuronal growth cones. J. Cell Biol. *158*, 139–152. https://doi.org/10.1083/JCB.200203038.
32. Bidone, T.C., and Odde, D.J. (2023). Multiscale models of integrins and cellular adhesions. Curr. Opin. Struct. Biol. *80*, 102576. https://doi.org/10.1016/J.SBI.2023.102576.
33. Koch, D., Rosoff, W.J., Jiang, J., Geller, H.M., and Urbach, J.S. (2012). Strength in the periphery: growth cone biomechanics and substrate rigidity response in peripheral and central nervous system neurons. Biophys. J. *102*, 452–460. https://doi.org/10.1016/J.BPJ.2011.12.025.
34. Kumarasinghe, U., Fox, L.N., and Staii, C. (2022). Combined traction force–atomic force microscopy measurements of neuronal cells. Biomimetics (Basel) *7*, 157. https://doi.org/10.3390/BIOMIMETICS7040157.
35. Betz, T., Koch, D., Lu, Y.B., Franze, K., and Käs, J.A. (2011). Growth cones as soft and weak force generators. Proc. Natl. Acad. Sci. USA *108*, 13420–13425. https://doi.org/10.1073/PNAS.1106145108.
36. Han, S.J., Oak, Y., Groisman, A., and Danuser, G. (2015). Traction microscopy to identify force modulation in subresolution adhesions. Nat. Methods *12*, 653–656. https://doi.org/10.1038/NMETH.3430.
37. Han, S.J., Azarova, E.V., Whitewood, A.J., Bachir, A., Guttierrez, E., Groisman, A., Horwitz, A.R., Goult, B.T., Dean, K.M., and Danuser, G. (2021). Pre-complexation of talin and vinculin without tension is required for efficient nascent adhesion maturation. Elife *10*, e66151. https://doi.org/10.7554/ELIFE.66151.
38. Oakes, P.W., Banerjee, S., Marchetti, M.C., and Gardel, M.L. (2014). Geometry regulates traction stresses in adherent cells. Biophys. J. *107*, 825–833. https://doi.org/10.1016/J.BPJ.2014.06.045.
39. Kulkarni, A.H., Ghosh, P., Seetharaman, A., Kondaiah, P., and Gundiah, N. (2018). Traction cytometry: regularization in the Fourier approach and comparisons with finite element method. Soft Matter *14*, 4687–4695. https://doi.org/10.1039/C7SM02214J.
40. Brangwynne, C.P., MacKintosh, F.C., Kumar, S., Geisse, N.A., Talbot, J., Mahadevan, L., Parker, K.K., Ingber, D.E., and Weitz, D.A. (2006). Microtubules can bear enhanced compressive loads in living cells because of lateral reinforcement. J. Cell Biol. *173*, 733–741. https://doi.org/10.1083/JCB.200601060.
41. Case, L.B., and Waterman, C.M. (2015). Integration of actin dynamics and cell adhesion by a three-dimensional, mechanosensitive molecular clutch. Nat. Cell Biol. *17*, 955–963. https://doi.org/10.1038/NCB3191.

42. Alfadil, E., and Bradke, F. (2023). Moving through the crowd. Where are we at understanding physiological axon growth? Semin. Cell Dev. Biol. *140*, 63–71. https://doi.org/10.1016/J.SEMCDB.2022.07.001.

43. Nichol, R.H., Hagen, K.M., Lumbard, D.C., Dent, E.W., and Gómez, T.M. (2016). Guidance of axons by local coupling of retrograde flow to point contact adhesions. J. Neurosci. *36*, 2267–2282. https://doi.org/10.1523/JNEUROSCI.2645-15.2016.

44. Atherton, J., Stouffer, M., Francis, F., and Moores, C.A. (2022). Visualising the cytoskeletal machinery in neuronal growth cones using cryo-electron tomography. J. Cell Sci. *135*, jcs259234. https://doi.org/10.1242/JCS.259234/VIDEO-3.

45. Webb, B.A., Aloisio, F.M., Charafeddine, R.A., Cook, J., Wittmann, T., and Barber, D.L. (2021). pHLARE: A new biosensor reveals decreased lysosome pH in cancer cells. Mol. Biol. Cell *32*, 131–142. https://doi.org/10.1091/MBC.E20-06-0383.

46. Charafeddine, R.A., Cortopassi, W.A., Lak, P., Tan, R., McKenney, R.J., Jacobson, M.P., Barber, D.L., and Wittmann, T. (2019). Tau repeat regions contain conserved histidine residues that modulate microtubule-binding in response to changes in pH. J. Biol. Chem. *294*, 8779–8790. https://doi.org/10.1074/JBC.RA118.007004.

47. Stehbens, S., Pemble, H., Murrow, L., and Wittmann, T. (2012). Imaging intracellular protein dynamics by spinning disk confocal microscopy. Methods Enzymol. *504*, 293–313. https://doi.org/10.1016/B978-0-12-391857-4.00015-X.

48. Wang, B., Shi, W., and Miao, Z. (2015). Confidence analysis of standard deviational ellipse and its extension into higher dimensional euclidean space. PLoS One *10*, e0118537. https://doi.org/10.1371/JOURNAL.PONE.0118537.

49. Jaqaman, K., Loerke, D., Mettlen, M., Kuwata, H., Grinstein, S., Schmid, S.L., and Danuser, G. (2008). Robust single-particle tracking in live-cell time-lapse sequences. Nat. Methods *5*, 695–702. https://doi.org/10.1038/nmeth.1237.

50. Dema, A., van Haren, J., and Wittmann, T. (2022). Optogenetic EB1 inactivation shortens metaphase spindles by disrupting cortical force-producing interactions with astral microtubules. Curr. Biol. *32*, 1197–1205.e4. https://doi.org/10.1016/j.cub.2022.01.017.

51. Dema, A., Rahgozar, S., Siquier, L., van Haren, J., and Wittmann, T. (2022). Controlling cell shape and microtubule organization by extracellular matrix micropatterning. Methods Mol. Biol. *2430*, 467–481. https://doi.org/10.1007/978-1-0716-1983-4_29.

52. Mustapha, F., SenGupta, K., and Puech, P.H. (2022). Protocol for measuring weak cellular traction forces using well-controlled ultra-soft polyacrylamide gels. Star Protoc. *3*, 101133. https://doi.org/10.1016/J.XPRO.2022.101133.

53. Wouters, O.Y., Ploeger, D.T.A., van Putten, S.M., and Bank, R.A. (2016). 3,4-dihydroxy-l-phenylalanine as a novel covalent linker of extracellular matrix proteins to polyacrylamide hydrogels with a tunable stiffness. Tissue Eng. Part C Methods *22*, 91–101. https://doi.org/10.1089/TEN.TEC.2015.0312.

## STAR★METHODS

### KEY RESOURCES TABLE

| REAGENT or RESOURCE | SOURCE | IDENTIFIER |
|---|---|---|
| Antibodies | | |
| Mouse monoclonal anti-DCX | Santa Cruz Biotechnology | sc-271390; RRID:AB_10610966 |
| Rabbit polyclonal anti-GFP | Invitrogen | A-11122, RRID:AB_221569; |
| Mouse monoclonal anti-MAPT(tau) E-4 | Santa Cruz Biotechnology | sc-515539 |
| Rat monoclonal anti-Tubulin (clone YL1/2) | Bio-rad | MCA77G (RRID: AB_325003) |
| Chemicals, peptides, and recombinant proteins | | |
| SPY-555 Tubulin | Spyrochrome / Cytoskeleton Inc. | CY-SC203 |
| SPY-555 FastAct | Spyrochrome / Cytoskeleton Inc. | CY-SC205 |
| SPY-650 FastAct | Spyrochrome / Cytoskeleton Inc. | CY-SC505 |
| SiR-Lysosome | Spyrochrome / Cytoskeleton Inc. | CY-SC012 |
| Alexa Fluor 568 Phalloidin | Thermo Fisher | A12380 |
| CellMASK Red | Thermo Fisher | H32712 |
| Paclitaxel | Thermo Fisher | P3456 |
| Matrigel hESC-Qualified Matrix | Corning | 354277 |
| mTeSR1 | STEMCELL Technologies | 85850 |
| Knockout DMEM/F12 | Thermo Fisher | 12660012 |
| DMEM/F-12, no phenol red | Thermo Fisher | 21041025 |
| Neurobasal-A Medium, no phenol red | Thermo Fisher | 12349015 |
| MEM Non-Essential Amino Acids Solution (100X) | Thermo Fisher | 11140050 |
| GlutaMAX Supplement | Thermo Fisher | 35050061 |
| N-2 Supplement (100X) | Thermo Fisher | 17502048 |
| B-27 Supplement (50X), serum free | Thermo Fisher | 17504044 |
| Poly-D-Lysine Hydrobromide | Sigma-Aldrich | A-003-E |
| Accutase | STEMCELL Technologies | 07920 |
| Y-27632 | STEMCELL Technologies | 72304 |
| Recombinant Human NT-3 (carrier-free) | BioLegend | 598202 |
| Human/Mouse/Rat BDNF, Animal-Free Recombinant Protein | Thermo Fisher | AF-450-02 |
| Laminin; Mouse | Corning | 354232 |
| Doxycycline hyclate | Thermo Fisher | J60579.14 |
| SU-8 photoresist | Kayaku Advanced Materials | N/A |
| 1-methoxy-2-propanol acetate (PGMEA) | Millipore Sigma | 484431 |
| trichloro(1H,1H,2H,2H-perfluorooctyl) silane | Millipore Sigma | 448931 |
| Krayden Dow Sylgard 184 Silicone Elastometer Kit | Fisher Scientific | NC9285739 |
| (3-aminopropyl) triethoxysilane | Millipore Sigma | 440140 |
| Aqueous Glutaraldehyde EM Grade 25% | Electron Microscopy Sciences | 16220 |
| 3,4-dihydroxy-L-phenylalanine | Millipore Sigma | D9628 |
| Critical commercial assays | | |
| Lipofectamine 3000 | Thermo Fisher | L3000001 |
| Lipofectamine Stem | Thermo Fisher | STEM00015 |
| jetOPTIMUS | Sartorius / Polypus | 101000006 |
| Experimental models: Cell lines | | |
| Retinal pigment epithelial (RPE) cells | Previously described in Wittmann et al.[30] | N/A |
| $I^3N$ human induced pluripotent stem cells (hiPSCc) | Previously described in Wang et al.[15] | N/A |

(*Continued on next page*)

*Continued*

| REAGENT or RESOURCE | SOURCE | IDENTIFIER |
|---|---|---|
| Recombinant DNA | | |
| pDCX-EGFP (wild-type and mutated) | This study | N/A |
| pSpCas9(BB)-2A-GFP | Feng Zhang | Addgene #48138 |
| pSpCas9(BB)-2A-GFP_DCX_exon7_gRNA1 | This study | N/A |
| pSpCas9(BB)-2A-GFP_DCX_exon7_gRNA2 | This study | N/A |
| pSpCas9(BB)-2A-GFP_DCX_exon1_gRNA1 | This study | N/A |
| pSpCas9(BB)-2A-GFP_DCX_exon1_gRNA2 | This study | N/A |
| pSpCas9(BB)-2A-GFP_DCX_exon1_gRNA3 | This study | N/A |
| pUC19_DCX_mEmerald_HDR | This study | N/A |
| mTagRFP-T-EB3-7 | Michael Davidson | Addgene #58012 |
| I3-01 nanocage plasmid | Matthew Akamatsu | Akamatsu et al.[19] |
| pmEmerald-I3-01 | This study | N/A |
| pmEmerald_mEmerald-I3-01 | This study | N/A |
| Software and algorithms | | |
| NIS Elements v5.3 | Nikon | https://www.microscope.healthcare.nikon.com/products/software/nis-elements |
| MATLAB R2023a | Mathworks | https://www.mathworks.com/products/matlab.html |
| u-track | Gaudenz Danuser, Khuloud Jaqaman | https://github.com/DanuserLab/u-track |
| TFM package | Sangyoon Han | https://sites.google.com/mtu.edu/hanlab/software |
| Fiji | Open Source | https://fiji.sc/ |
| Microsoft Excel | Microsoft | https://www.microsoft.com/en-us/ |
| Adobe Creative Suite | Adobe | https://www.adobe.com/creativecloud.html |
| Deposited data | | |
| Microscopy data and data analysis related to Figures 1, 2, 3, and 4 and S1–S4 | This paper | https://doi.org/10.5061/dryad.8sf7m0d01 |
| Other | | |
| 35 mm glass-bottom dishes (No. 1.5 cover glass) | Mattek | P35G-1.5-20-C |
| 12-well glass bottom plate (No. 1.5 cover glass) | Cellvis | P12-1.5H-N |
| 76.2 mm Silicon Wafers | University Wafer | 695 |
| Far-red 200 nm polystyrene beads | Bangs Laboratories | FSFR002 |

## EXPERIMENTAL MODEL AND SUBJECT DETAILS

### Cell lines and cell culture

Retinal pigment epithelial (RPE) cells were cultured and authenticated as previously described.[45] i$^3$N hiPSCs were cultured and differentiated into cortical i$^3$Neurons as previously described,[15,16] with a 3-day pre-differentiation step. Of note, i$^3$N cells are male and thus only have one copy of the DCX gene.

## METHOD DETAILS

### Molecular cloning

DCX missense mutations were produced by QuickChange II (Agilent) site directed mutagenesis of a wildtype DCX-EGFP plasmid. Plasmids in which multiple cdk5 phosphorylation sites in the DCX C-terminus were replaced with non-phosphorylatable or phosphomimetic residues were cloned by Gibson assembly (New England Biolabs) of a synthetic DNA fragment carrying these changes (synthesized by Twist Biosciences) into the DCX-EGFP plasmid cut with EcoRV and SalI.

I3 nanocage constructs tagged either with a single or a tandem repeat mEmerald at the N-terminus were constructed by Gibson assembly with PCR products encoding mEmerald and a mammalian codon optimized I3-01 K129A sequence from a plasmid

obtained from M. Akamatsu[19] into a pEGFP-N1 backbone. Of note, we tested different mEmerald-tagged I3-01 nanocage constructs and found that attaching mEmerald to the I3-01 C-terminus abolished nanocage assembly. All constructs were verified by whole plasmid sequencing (Primordium Labs).

### i$^3$N genome editing

To insert mEmerald at the C-terminus of the endogenous DCX locus, cells were co-transfected with a mixture of pSpCas9(BB)-2A-GFP plasmids (gift from Feng Zhang; Addgene plasmid #48138) containing two different sgRNA sequences (TTGGATGACTC GGACTCGCT and CGCTTGGTGATTCCATGTAA) targeting the DCX exon 7 just before the stop codon and a pUC19 HDR template including the mEmerald coding sequence at the C-terminus of DCX. Because DCX is only expressed during neuron development and not in hiPSCs, to select DCX-mEmerald i$^3$N clones, individual colonies were picked into duplicate glass-bottom plates and mEmerald-expressing clones were identified by spinning disk confocal microscopy. Out of 24 colonies, we isolated one DCX-mEmerald expressing line.

To generate the DCX −/Y i$^3$N line, DCX-mEmerald i$^3$N cells were transfected with a mixture of three pSpCas9(BB)-2A-GFP plasmids containing sgRNA sequences in exon 1 (AAGGTACGTTTCTACCGCAA, GCGGTAGAAACGTACCTTCT and ATGGG GACCGCTACTTCAAG). DCX −/Y i$^3$N cells have a 22 base pair deletion and frame shift at position 157 (…AAGAAAGCCaagaagg tacgtttctaccgcaATGGGGAC…; lower case indicates the deleted sequence.) All i$^3$N genome editing was confirmed by genomic PCR and sequencing of the PCR amplicon as well as immunoblotting for DCX protein. Genomic DNA was isolated using a Purelink Genomic DNA Mini Kit (ThermoFisher).

### Antibodies

Mouse monoclonal anti-DCX: Santa Cruz Biotechnology Cat# sc-271390, RRID:AB_10610966; Rabbit polyclonal anti-GFP: Invitrogen Cat# A-11122, RRID:AB_221569; Mouse monoclonal anti-MAPT(tau) E-4, sc-515539; Santa Cruz Biotechnology, no RRID available.[46] For immunoprecipitation, DCX-mEmerald i$^3$Neurons were lysed in 50 mM Tris-HCl pH 7.5, 100 mM NaCl, 10% glycerol and 0.5% Triton-X100 with protease and phosphatase inhibitors. The lysate was cleared by centrifugation at 14000 rpm, incubated with anti-GFP loaded Affi-Prep Protein A Resin (Biorad), and after washing DCX-mEmerald protein was eluted in SDS sample buffer. The DCX-mEmerald band at around 70 kDa was excised from the gel and phosphorylated residues were determined by mass spectrometry (MS Bioworks LLC).

### Live microscopy and image analysis

Unless otherwise noted, i$^3$Neuron live microscopy was performed 1-2 days after replating pre-differentiated i$^3$N cells onto laminin-coated glass-bottom dishes (Mattek) essentially as described.[16] SPY555 tubulin, a cell-permeable fluorogenic taxane derivative, and SPY555- or SPY650-FastAct (Spyrochrome), cell-permeable fluorogenic jasplakinolide derivatives, were added to i$^3$Neurons at a 1:2000 and 1:3000 dilution approximately 30 min before imaging, and cells were discarded after a maximum of 3 hours. SiR-lysosome (Spirochrome), a cell-permeable and lysosome-specific[45] far-red-tagged pepstatin A that binds cathepsin D, was used at a 0.5-1 μM concentration. Similarly, RPE cells were plated on uncoated, plasma-cleaned glass-bottom dishes and transiently transfected using Lipofectamine 3000 (Thermo Fisher) or jetOPTIMUS (Sartorius).

All live microscopy was performed either with a Yokogawa CSU-X1 spinning disk confocal essentially as described[47] or, for most i$^3$Neuron microscopy, with a CFI Apochromat TIRF 60X NA 1.49 objective (Nikon) on a Yokogawa CSU-W1/SoRa spinning disk confocal system, and images acquired with an ORCA Fusion BT sCMOS camera (Hamamatsu) controlled through NIS Elements v5.3 software (Nikon). For high-resolution imaging of dim signal, SoRa mode was combined with 2x2 camera binning resulting in an image pixel size of 54 nm.

To determine the relative amount of MT-bound DCX in transfected RPE cells, intensity profiles perpendicular to DCX-coated MTs were fitted with a 1D Gaussian function in Matlab and the MT-bound fluorescence estimated as the integral over two standard deviations from the mean (μ +/- 2σ). The amount of DCX in the same volume of cytoplasm was estimated as $4\sigma(\text{offset}_{\text{Gaussian}}-\text{offset}_{\text{Camera}})$ as indicated in Figure S1A. Lastly, the ratio of MT-bound to cytoplasmic DCX signal for all mutated DCX constructs was normalized to the wild-type DCX MT-to-cytoplasm ratio. A similar approach was used to measure tubulin or DCX-mEmerald fluorescence along straight and curved growth cone MT segments or neurite MT bundles by integrating intensity profiles perpendicular to neurite MT bundles or individual growth cone MTs. Of note, we likely overestimate remaining DCX-binding to neurite shaft MTs because, in contrast to individual growth cone MTs, we cannot distinguish MT-bound from cytoplasm fluorescence in the neurite shaft.

To determine the absolute number of DCX molecules on growth cone MTs, we first constructed a calibration curve from RPE cells transiently transfected with I3-01 nanocage constructs labelled with either 60 or 120 mEmerald molecules. 2D Gaussian functions were fitted to individual nanocage dots using an interactive Matlab code and the nanocage intensity measured in a circle with a two standard deviation radius around the center of the fit minus the offset of the Gaussian function in the same area (Figure S3C). Because the 2σ circle encompasses 86.47% of the volume of a 2D Gaussian,[48] the measured nanocage intensities were divided by 0.8647 to estimate the total intensity for each nanocage point spread function. DCX-mEmerald intensity along growth cone MTs was measured in 14-pixel wide rectangles, corrected for local background (Figure S3D), and the number of DCX-mEmerald molecules was calculated using the nanocage calibration curve. Importantly, mEmerald tagged nanocage and DCX-mEmerald i$^3$Neuron images were acquired using CSU-W1/SoRa super-resolution spinning disk microscopy (240x magnification; 27 nm image pixel size)

during the same imaging session to minimize day-to-day instrument variability with identical 488 nm 500 ms exposures with 50% laser power, which on our system corresponds to ~150 mW $mm^{-2}$. We chose this relatively high light intensity to obtain images with superior signal-to-noise ratios and minimized the number of acquired images to avoid photobleaching as much as possible.

Lysosome velocity in $i^3$Neurons was tracked in MATLAB using the u-track package (https://github.com/DanuserLab/u-track)[49] with Gaussian mixture model detection, allowing directed motion propagation and an increased search radius upper bound of 40–60 pixels to enable tracking of fast lysosome movements. Frame-to-frame velocities were extracted from the 'tracksFinal' structure as described,[50] and frame-to-frame displacements of less than 2 pixels (i.e. 108 nm) were excluded from further analysis.

Growth cone MT ends in SPY555-tubulin labeled $i^3$Neurons plated on laminin-coated glass-bottom dishes were tracked manually using the 'Segmented Line' tool in FiJi. MT growth and shortening rates were calculated for frame-to-frame displacements greater than 3 pixels (i.e. 160 nm). Displacements below that threshold were classified as a pause.[30] Kymographs to measure retrograde F-actin flow were generated as described.[16]

## Chemotaxis assay

Molds to cast polydimethylsiloxane (PDMS) chemotaxis chambers were generated by photolithography on an Alveole PRIMO UV-micropatterning system[51] in two exposure steps. First, a thin layer (3-5 μm) of SU-8 2005 (Kayaku Advanced Materials) was spin-coated onto a dehydrated silicon wafer and the 10 μm microchannels were exposed with a 20x objective and a radiant exposure of 6 $mJ/mm^2$ with 20% laser power and no stitching in the PRIMO Leonardo software. After post-exposure bake, a 120 μm SU-8 2100 layer was spin-coated on top of the first layer. Using 540 nm reflected light, the exposed microchannels were aligned to the mask of the media and cell channels and exposed using a 4x objective with 3 $mJ/mm^2$ radiant exposure and 100% laser power. Pre- and post-exposure bakes were according to the manufacturer's specifications. The exposed SU-8 wafer was developed in 1-methoxy-2-propanol acetate (PGMEA) following standard protocols and rendered hydrophobic by overnight vapor deposition of trichloro(1H,1H,2H,2H-perfluorooctyl) silane. Chemotaxis chambers were cut from Sylgard 184 PDMS casts directly onto the SU-8 wafer or plastic replicas from the first, silane-contaminated PDMS cast. To remove unpolymerized PDMS, chemotaxis chambers were washed overnight in isopropanol and multiple dimes in $ddH_2O$. Dried, plasma-cleaned[51] PDMS tiles were adhered to plasma-cleaned #1.5 coverslips and the assembly baked for 30 min at 100°C, washed in ethanol, dried, UV-sterilized and filled with 50 μg/ml poly-D-lysine in PBS, incubated for 30 min at 37°C, flushed three times with PBS and then filled and incubated with 50 μg/ml mouse laminin in PBS for 30 min, and finally flushed with maturation medium.[16] Pre-differentiating $i^3$Ns were seeded in the central channel at a concentration of $10^6$ cells in 100 μl maturation medium without BDNF, and the medium in one of the side channels was replaced with complete maturation medium containing 10 ng/ml BDNF and 25 μg/ml fluorescent dextran. Stitched images of $i^3$Neurons were acquired 2-4 days after seeding in both phase contrast (to count neurites that have passed through the microchannels) and fluorescence (to visualize the gradient).

## Traction force microscopy

For traction force microscopy (TFM), 400 Pa polyacrylamide gels were cast in 20 mm glass-bottom dishes (Mattek) essentially following a recent, detailed protocol.[52] Briefly, plasma-cleaned glass-bottom dishes were incubated with 40 μl 0.5% (3-aminopropyl) triethoxysilane for 30 min with agitation, washed three times with $ddH_2O$, incubated with 80 μl 0.5% glutaraldehyde, washed three times with $ddH_2O$ and dried. 400 Pa polyacrylamide gels were prepared by mixing 147.6 μl $ddH_2O$, 10 μl 20x PBS, 15 μl 40% acrylamide, 5 μl 2% bis-acrylamide, 2.4 μl far red fluorescent 200 nm polystyrene beads (Bangs Laboratories FSFR002), 20 μl fresh 1% ammonium persulfate and 0.2 μl tetramethyl ethylenediamine. 10 μl gel solution was added per glass-bottom dish and the solution covered with an 18 mm round plasma-cleaned and trichloro(1H,1H,2H,2H-perfluorooctyl) silane-treated coverglass. The glass-bottom dishes were flipped upside down to allow the beads to sediment toward the top of the gel and polymerized for 1 hour in a humidified chamber in the dark. After polymerization the dishes were incubated for at least 10 min in $ddH_2O$ to facilitate removal of the silanized coverglass. The gel surface was then activated by incubating with 1 ml 2 mg/ml 3,4-dihydroxy-L-phenylalanine (L-DOPA) dissolved in 10 mM Tris-HCl pH 10 for at least 30 min,[53] washed once with 10 mM Tris-HCl pH 10 and three times with PBS. The gels were coated with 200 μl of 100 μg/ml mouse laminin for at least 30 min at 37°C in a tissue culture incubator, washed with PBS and sterilized for 5 min with UV light in a biosafety cabinet before plating $10^5$ $i^3$Neurons in complete maturation medium.

TFM time-lapse sequences were acquired on a CSU-W1/SoRa spinning disk confocal with a long working distance 40x 1.15 N.A. water immersion objective (MRD77410) in super-resolution mode resulting in an effective pixel size of 40.5 nm. Stress-free, decellularized reference images were acquired 15 min after treatment with 1% Triton X-100. TFM data were analyzed using the fast boundary element method (FastBEM) with L1 regularization[36] (https://github.com/DanuserLab/TFM), which has improved noise suppression without underestimating traction magnitude compared with older FFT-based TFM analysis. Because FastBEM is computationally intensive, original 16-bit bead images were converted to 8-bit and downsampled by 50%. After subpixel alignment to the reference image, displacement fields were calculated with high-resolution bead subsampling and subpixel correlation and the following parameters: alpha value: 0.01; template size: 21 pixel; maximum displacement: 31 pixel. For each time-lapse sequence the optimal L1 regularization parameter was determined for the first frame and the same parameter used for all subsequent frames. This automatically determined L1 regularization parameter was between $10^{-2}$ and $10^{-4}$ for all datasets. To calculate the root mean square traction stress per growth cone, the growth cone CellMask image threshold was dilated by 1.2 μm because the displacement field extends beyond the growth cone edge. Assuming that displacement and force field vectors

are largely aligned, the strain energy was estimated by the product of the magnitude of the displacement and force field maps divided by 2.

## QUANTIFICATION AND STATISTICAL ANALYSIS

Details of statistical analysis including the type of test, p-values and numbers of biological replicates are provided within the relevant figures and figure legends. All statistical analysis was done in MATLAB (Mathworks, Inc.)., and graphs were produced in MATLAB and in Excel (Microsoft). In all figures, box plots show median, first and third quartile, with whiskers extending to observations within 1.5 times the interquartile range. No randomization, stratification or sample size estimation strategies have been employed. Unless indicated otherwise, all data points from a given experiment were analyzed, and a $p < 0.01$ is considered statistically significant. For every experiment reported, at least 3 biological replicates with similar results were performed.